magnetochemistry

MDPI

Article

Spin-Filter Magnetic Tunnel Junctions Based on A-Type Antiferromagnetic CrSBr with Giant Tunnel Magnetoresistance

Hao Liu [1,2], Yue-Yang Liu [1,*], Hongyu Wen [1,*], Haibin Wu [1], Yixin Zong [1], Jianbai Xia [1,2] and Zhongming Wei [1]

[1] State Key Laboratory of Superlattices and Microstructures, Institute of Semiconductors, Chinese Academy of Sciences, Beijing 100083, China
[2] Center of Materials Science and Optoelectronics Engineering, University of Chinese Academy of Sciences, Beijing 100049, China
* Correspondence: yueyangliu@semi.ac.cn (Y.-Y.L.); wenhongyu@semi.ac.cn (H.W.)

Abstract: CrSBr is a stable two-dimensional (2D) van der Waals (vdW) magnet with intralayer ferromagnetic and interlayer antiferromagnetic couplings. Here, we propose to use CrSBr as the barrier in spin-filter (sf) MTJ and establish the devices based on graphene/CrSBr/graphene structures. Employing density functional theory (DFT) combined with the nonequilibrium Green's function approach, we investigated the transmission details, and the results show TMR values above 330%, 2×10^7% and 10^5% with two-, four- and six-layer CrSBr at zero bias, respectively. Subsequently, we systematically analyze the transmission spectra, transmission eigenstates, electrostatic potentials, band structures and local density of states to elaborate the underlying mechanism of the TMR effect in the sf-MTJs. Our results indicate the great prospect of CrSBr-based sf-MTJs in applications, and provide guidance for futural experiments.

Keywords: spin-resolved magnetic tunnel junction; A-type antiferromagnetic material; giant tunnel magnetoresistance; transmission analysis

Citation: Liu, H.; Liu, Y.-Y.; Wen, H.; Wu, H.; Zong, Y.; Xia, J.; Wei, Z. Spin-Filter Magnetic Tunnel Junctions Based on A-Type Antiferromagnetic CrSBr with Giant Tunnel Magnetoresistance. *Magnetochemistry* **2022**, *8*, 89. https://doi.org/10.3390/magnetochemistry8080089

Academic Editor: Roberto Zivieri

Received: 28 July 2022
Accepted: 8 August 2022
Published: 11 August 2022

1. Introduction

Since the tunnel magnetoresistance (TMR) effect was observed in Co/Ge/Fe by Julliere in 1975 [1], the technology of magnetic tunnel junctions (MTJs) on the basis of the TMR effect has developed over a long period of time. MTJs are normally sandwich structures consisting of two ferromagnetic (FM) layers on both sides and an insulating non-magnetic tunneling barrier layer in the middle [2]. When the two FM layers present parallel/antiparallel magnetization configurations (PC/APC), the transmission of carriers displays significant distinction, so the electrical resistivity of MTJs could be regulated by an external magnetic field [3,4].

Giant magnetoresistance (GMR) devices have a structure similar to that of MTJs other than the fact that there are conducting rather than insulating layers in the middle of GMR devices. GMR systems are usually multilayer and stacked to improve this characteristic [5]. Spin valve sensors based on the GMR effect are applied in information technology, automotive applications and biosensors [6]. The improvement in storage density requires good scalability and a high sensitivity of sensor elements; therefore, a lot of research has ensued, with studies on low-field applications [7], amorphous materials [8], etc. [9]. However, MTJs are higher in sensitivity and lower in energy compared to GMR devices, and they have thus been rapidly and creatively applied in magneto-resistive memories and sensors [3,4,10–12].

To downsize the devices and improve their performances, 2D materials that have smooth interfaces and atomic-level thickness control [13] are considered for fabricating MTJs [14,15]. Additionally, the discovery of 2D intrinsic magnets—$Cr_2Ge_2Te_6$ [16], CrI_3 [17], Fe_3GeTe_2 [18] etc. [19]—has opened a promising avenue to establish 2D MTJs. Two-dimensional vertical MTJs are a kind of 2D heterojunction which can be epitaxially grown on a substrate layer by vdW forces. They have better interface quality and a smaller size than traditional MTJs with MgO [20], AlO_x barrier [21] and bulk FM layers.

A schematic diagram of a common MTJ is presented in Figure 1a, in which a pining layer is significant to maintain the magnetization in the fixed FM layer [22,23]. Only the magnetization of a free layer can be modulated by an external field, so that people can control MTJs to reach PC and APC. Additionally, a layer of tunnel barrier is necessary to filter the electrons and decouple the magnetism of two FM layers [24,25]. In 2000, taking advantaging of the spin filter effect, a new kind of MTJ device was proposed, called the spin-filter MTJ (sf-MTJ) [26]. It only consists of four layers (as shown in Figure 1b): two normal electrodes and two FM and insulating layers with different coercivities. An external field can only flip the magnetic moment of the layer with smaller coercivity so that the sf-MTJ can switch between the PC and APC with different conductivities [27]. The sf-MTJs have the potential to work in a small field, above room temperature and to possess larger sensitivity [26].

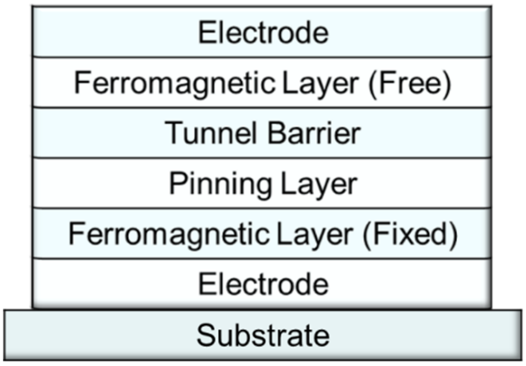

(**a**)

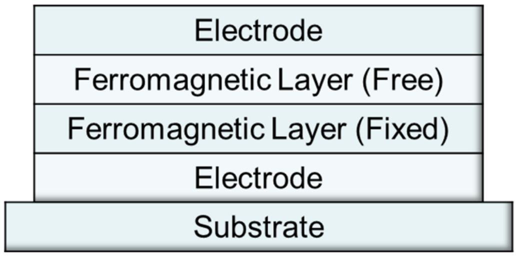

(**b**)

Figure 1. The schematic diagrams of different MTJs: (**a**) A common MTJ; and (**b**) A spin-filter MTJ.

Two-dimensional CrI_3 multilayers were recently adopted to design and fabricate sf-MTJs in laboratory [28]. The two-dimensional CrI_3 multilayer has an A-type magnetic order [29], which means that its intralayer coupling is FM while its interlayer coupling is antiferromagnetic (AFM) [30]. Figure 2a presents an A-type AFM bilayer with an intralayer FM order but interlayer AFM coupling, where the two layers have opposite magnetic moments. A large enough external in-plane (out-of-plane) magnetic field can switch the interlayer coupling from an interlayer AFM to FM order [28], meaning that the magnetization changes from antiparallel to parallel, as shown in Figure 2b (the magnetization in a large in-plane magnetic field) and Figure 2c (the magnetization in a large out-of-plane magnetic field). As a result, we can employ the A-type AFM multilayer instead of FM layers with different coercivities to design sf-MTJ. Of course, the A-type layers must be insulators or semiconductors because they also work as tunnel barriers.

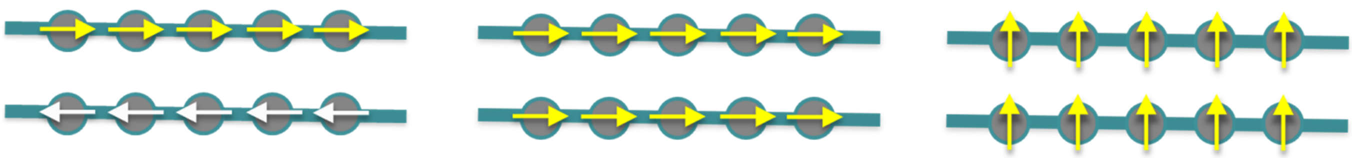

(**a**) (**b**) (**c**)

Figure 2. (**a**) A-type AFM bilayer with intralayer FM order and interlayer AFM order; (**b**) A-type AFM bilayer in an external in-plane magnetic field; (**c**) A-type AFM bilayer in an external out-of-plane magnetic field. Different external field can change the interlayer coupling into in-plane FM in 2 (**b**) or out-of-plane FM in 2 (**c**).

The TMR value, which is defined as $(G_P - G_{AP})/(G_{AP}) \times 100\%$, is usually used to express the gap between the conductance of an MTJ under PC (G_P) and APC (G_{AP}). A TMR up to 19,000% has been observed in the 2D CrI_3 sf-MTJ [28], which is an order of magnitude larger than the TMR in MgO MTJs [25,31]. The results have strongly confirmed the advantage of sf-MTJs based on 2D A-type AFM materials.

In addition to CrI_3, there exist many other 2D A-type AFM materials, such as $CrCl_3$ [32] and $MnBi_2Te_4$ [33] in experimental observations and $YTiO_3$ [34], in first-principle calculations. Among them, CrSBr is a 2D A-type AFM semiconductor with a band gap of approximately 1.5 eV [35]. Bulk CrSBr single crystals can be grown from Cr and S_2Br_2 by chemical vapor transport or other methods for obtaining metallic alloys [36,37] and the monolayer CrSBr flake can be easily exfoliated due to the interlayer vdW forces [35,38]. CrSBr has a high Néel temperature ($T_N \sim 140$ K), which allows the realization of 2D spintronic devices in experiments [38,39]. In addition, unlike metals and oxide compounds [40,41], most 2D magnetic materials tend to degrade in air through oxidation or hydration [16,17,42] but CrSBr is stable in air so that it may be stored under ambient conditions for one month without degradation [39]. In short, CrSBr is air-stable, has a relatively high Néel temperature and shows semiconductor characteristics with a band gap approximately 1.5 eV, allowing many methods to manipulate the magnetism [38]. It is thus a proper candidate to investigate and reveal the spin-resolved transmission at a low dimension. Therefore, we propose to employ multilayer CrSBr to design sf-MTJs in this work and investigate the transmission performances by DFT. These studies provide a promising direction for the future MTJ design.

2. Results

First of all, we built and optimized the supercell of a 2D layered CrSBr (the details of structural relaxation and electronic structure calculation are given in Section 4: Materials and Methods).

The optimized structure is exhibited in Figure 3a with three views, in accordance with the former experiments [35,43]. After that, we employed even numbers of CrSBr layers (two, four and six layers) and graphene to model the sf-MTJs with a lattice mismatch of 6.75% and completed the device optimization. Taking the bilayer CrSBr, for instance, as shown in Figure 2b, the MTJ consists of graphene electrode, the central transmission region of bilayer CrSBr and another graphene electrode along the c axis, which is also the direction of electron transmission in simulation. The two graphene electrodes are semi-infinite. Considering the vdW forces through the DFT-D3 method [44], it turns out that the distance is 3.41 Å between CrSBr layers and 3.25 Å between CrSBr and graphene, indicating the weak combinations. Figure 3c provides sf-MTJs specifically with two/four/six-layer CrSBr, where the central regions are demarked by black lines and the electrodes are squared by red lines. The 2D CrSBr is herein perceived as layers without defects, deformation and degradation, which may affect the performance in transmission in real devices [45,46]. In the experiment, sf-MTJs are usually encapsulated by a hexagonal BN to improve the quality of the interface and avoid degradation [28]. However, hexagonal BN does not influence the transmission performance in calculations without current flowing through, so only the internal space in encapsulation is considered in our work.

Subsequently, the transmission probabilities in different transverse Bloch wave vectors (referred to as transmission spectra in the following texts) at zero bias of the three sf-MTJs are calculated and we deduced the conductance (G_P and G_{AP}) and TMR values, exhibited in Table 1. The sf-MTJ with two, four and six-layer CrSBr have a TMR of approximately 330%, 2×10^7% and 10^5%, respectively. Compared with two-layer sf-MTJ, the TMR of the four-layer sf-MTJ dramatically increases from 10^2% to 10^7% orders of magnitude. We notice that the increase comes from the change in G_{AP}, which is much smaller in the four-layer sf-MTJ than that in the two-layer. In the six-layer device, the value of G_{AP} does not show a significant change while G_P becomes much smaller on account of its increasing thickness, resulting in the decrease in TMR. In conclusion, the sf-MTJ with graphene electrodes and four-layer CrSBr has a giant TMR, making it a promising device model in future experiments and applications, adding to the other aforementioned advantages of CrSBr.

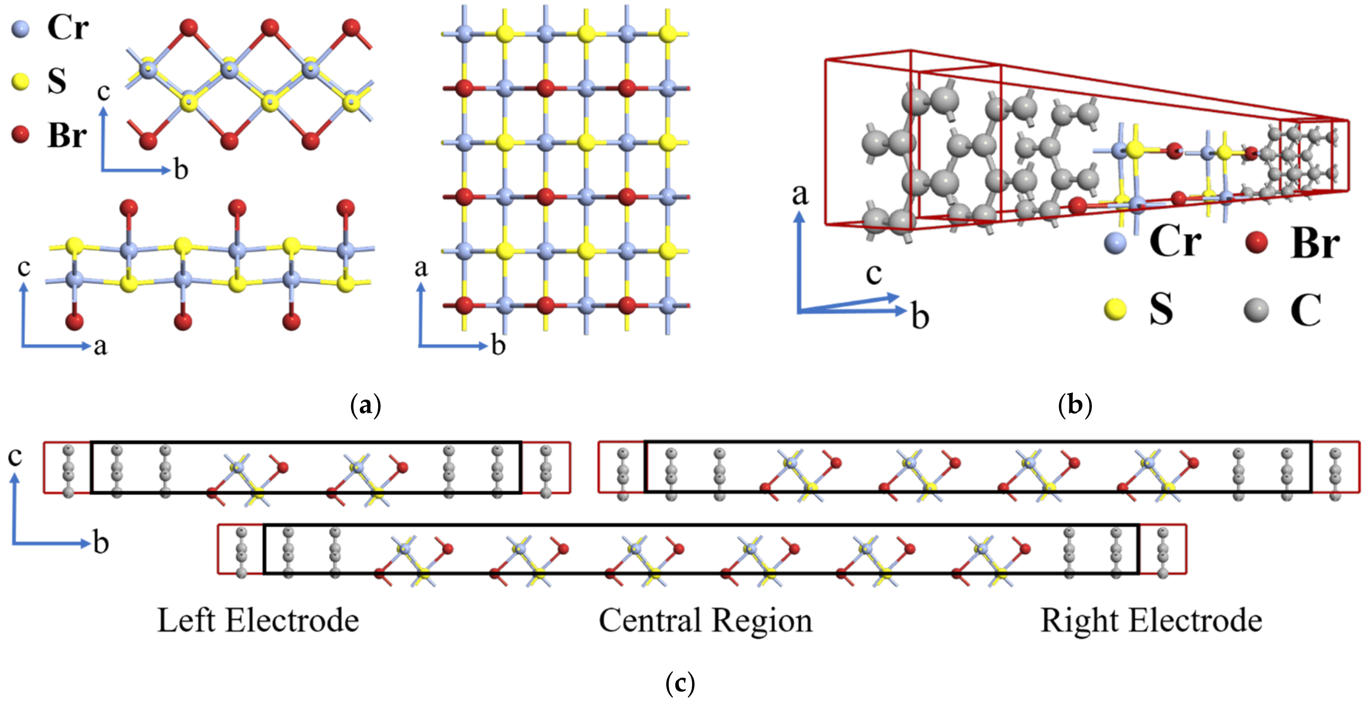

Figure 3. (**a**) Structure of monolayer CrSBr (3 × 3) viewed along the a axis, b axis and c axis. Cr, S and Br atoms are colored in blue, yellow and red, respectively; (**b**) The perspective view diagram of a graphene/bilayer CrSBr/graphene sf-MTJ device. C atoms are colored in gray; (**c**) The device model based on the 2/4/6-layer CrSBr. The red and black squares represent electrodes and central regions, respectively.

Table 1. The values of G_P (the 2nd column), G_{AP} (the 3rd column) and TMR (the 4th column) of MTJs with different numbers of CrSBr layers through calculations.

Number of CrSBr Layers	G_P (Siemens)	G_{AP} (Siemens)	TMR
2	4.35×10^{-10}	1.01×10^{-10}	$3.3 \times 10^{2}\%$
4	1.87×10^{-12}	9.19×10^{-18}	$2.0 \times 10^{7}\%$
6	7.52×10^{-14}	6.86×10^{-17}	$1.1 \times 10^{5}\%$

We will then make a detailed analysis and interpretation of the CrSBr-based sf-MTJs to explain the causes and mechanism of giant TMR and the performance variation of different numbers of layers in the following section: Discussion.

3. Discussion

First of all, the transmission spectra are indispensable in the analysis of MTJs, because the spectra contain plenty of information about the transmission of charge carriers. Different spins of electrons and different magnetizations result in different scattering. Four transmission spectra of the sf-MTJ with two-layer CrSBr are exhibited in Figure 4. Figure 4a,b are the majority and minority spin states, hereinafter referred to as the up (↑) and down (↓) states, in PC (the magnetic moments are parallel), while Figure 4c,d are the up and down states in APC. The horizontal axis (k_a) and vertical axis (k_b) are momentums in reciprocal space in parallel to the cross-sectional direction of the c axis. The various colors from blue to red in the spectra represent transmission probabilities from low to high.

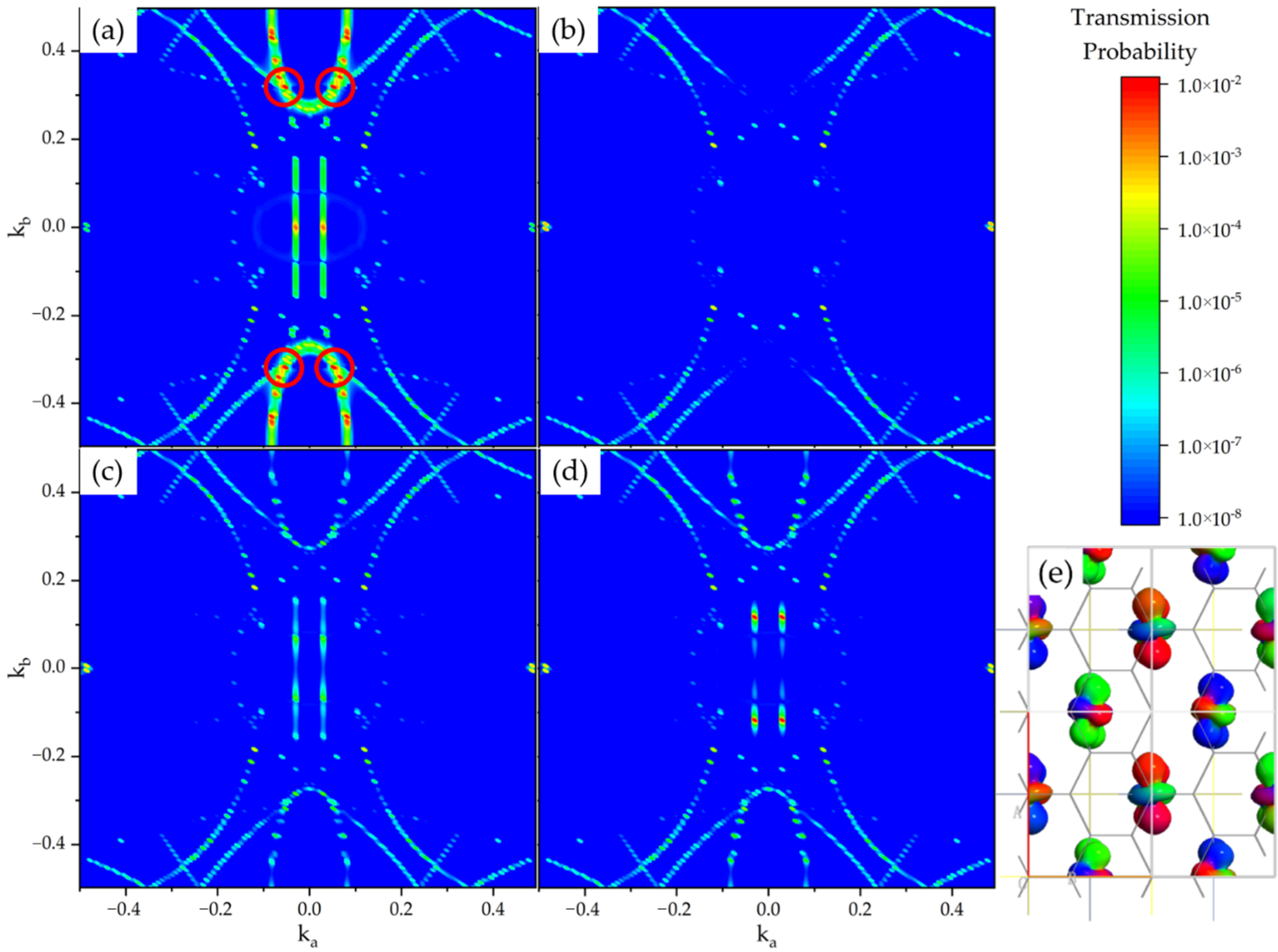

Figure 4. The transmission spectra (transmission probabilities of electrons with different transverse Bloch wave vectors) of (**a**) Majority spin states in PC; (**b**) Minority spin states in PC; (**c**) Majority spin states in APC; and (**d**) Minority spin states in APC. The colors represent different transmission probabilities with a logarithmic for presenting more information. (**e**) The transmission eigenstates of the spots with the highest probability in (**a**,**b**) are from a c axis perspective. The figures are the calculated results of the modeling.

Before we start analyzing the spectra, we divide the transmission electrons in different orbitals and symmetries into four types as usual, according to the similar transmission performance: $\Delta_1(s,\ p_z, d_{z^2})$ with spherical symmetry, $\Delta_5(p_x, p_y, d_{xz}, d_{yz})$ with two-fold symmetry, $\Delta_2\left(d_{x^2-y^2}\right)$ and $\Delta_{2'}(d_{xy})$ with other symmetries [47]. For instance, MgO emerged as a barrier material because of the filtering characteristics for Δ_1 electrons [48]. In the spectra, Δ_1 electrons should surround the origin, Δ_5 and Δ_2 electrons should distribute around $k_a = 0$ or $k_b = 0$, and Δ_2 electrons distribute around the diagonals.

In the transmission, the spots with the highest probabilities dominate the performance. In general, Figure 4a shows a relatively higher transmission probability of up spin in PC than the other three circumstances, which is consistent with the spin-resolved scattering in MTJs. The differences indicate that up spin electrons in PC have a higher transmission than other three circumstances, which leads to the obvious TMR effect.

The four highest transmission spots are circled in red in Figure 4a and are located near the $k_a = 0$ axis, meaning that Δ_5 or Δ_2 electrons have the best transmission performance in the two-layer CrSBr-based sf-MTJ. For a better understanding of the dominant electrons in the transmission, the eigenstates in the transmission are calculated and drawn in Figure 4e. The eigenstates mainly surround magnetic atoms Cr. It is obvious that the eigenstates have four nodes. The cloud structures belong to the $d_{x^2-y^2}$ electron, so we can deduce that Δ_2 electrons dominate the transmission in the sf-MTJ with the two-layer CrSBr.

However, it should be noted that the TMR of the two-layer device is not high (330%). The TMR dramatically increases when the CrSBr barrier change from two layers to four layers. It can be recognized from Table 1 that the most significant difference between the four layers and two layers—other than TMR values—is G_{AP}, which is seven orders of magnitude less. As a result, we can qualitatively declare that the giant TMR with four-layer CrSBr originates from the strong scattering in APC. When there are only two layers in the middle of the sf-MTJ, the device does not possess adequate filtration in APC. The bilayer CrI_3 sf-MTJ shows a good characteristic [28] because CrI_3 is insulating but CrSBr is a semiconductor.

Another point of concern is that the transmission spectra of up states and down states in APC (Figure 4c,d) are not the same, indicating that the two spin states are scattered differently. Clearly, Figure 4d has some red spots with higher transmission probabilities than Figure 4c. The phenomenon is not common in MTJs and leads to the higher level of G_{AP} with bilayer CrSBr, so we investigated the spin-resolved band structure and electrostatic potentials of bilayer CrSBr to explain the phenomenon.

Through the hybrid functional method [49], the electrostatic potentials of bilayer CrSBr are obtained and displayed in Figure 5, where Figure 5a is the potential in PC and Figure 5b is that in APC. To more intuitively illustrate the figures, we labeled the locations of the conduction band minimum (CBM) of up and down spin instead of placing the diagrams of band structures. The vacuum level is set to 0 eV (E_{VAC} in Figure 5). The CBM of up/down spin is labeled by $E_{CBM\uparrow}/E_{CBM\downarrow}$. Electron affinity is defined as the difference between the vacuum and CBM, labeled by $E_{ea\uparrow}$ or $E_{ea\downarrow}$ with a different spin.

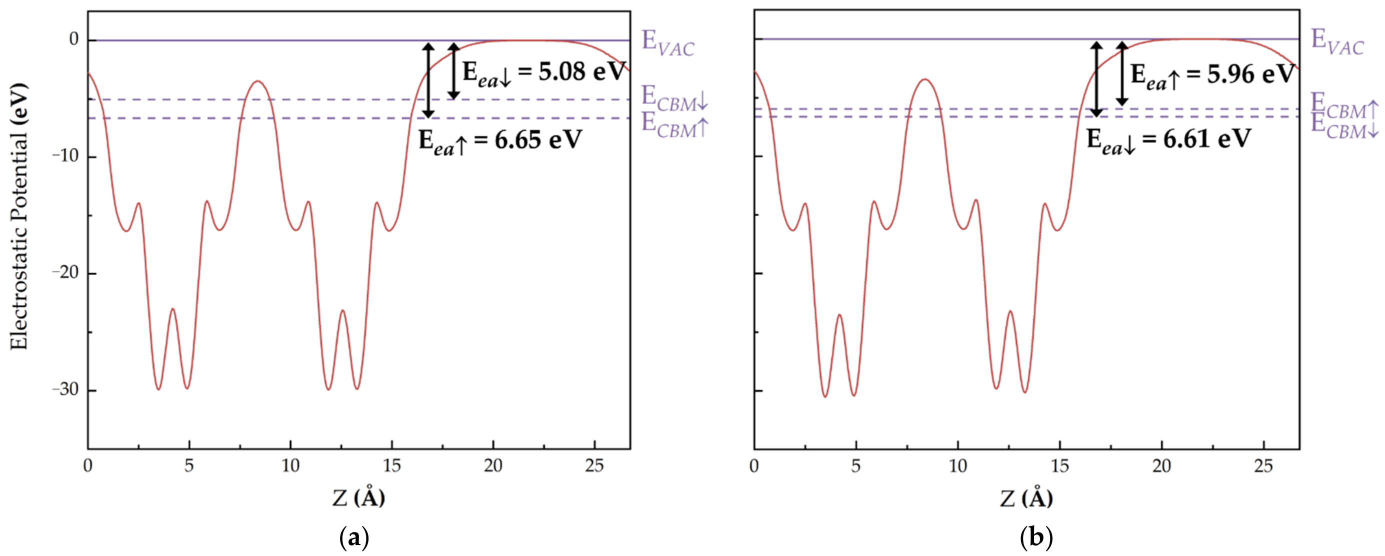

Figure 5. (**a**) The electrostatic potential of the bilayer CrSBr in PC; and (**b**) The electrostatic potential of bilayer CrSBr in APC. The location of the vacuum energy level is marked by a blue solid line, and the energy levels of CBM are marked by blue dashed lines. The horizontal axis represents the position in the direction of transmission. The thickness of the vacuum is 10 Å. The figures are the calculated results of the modeling.

The work function of the graphene electrode (W_{Gr}, defined as the difference between the vacuum and Fermi level) is also calculated for comparison. It turns out that the W_{Gr} is 2.87 eV, which is obviously smaller than $E_{ea\uparrow}$ and $E_{ea\downarrow}$ in PC and APC. As a result, the electrons will transfer from graphene to CrSBr in the sf-MTJ with bilayer CrSBr. However, the up and down states are not equivalent because $E_{ea\uparrow}$ and $E_{ea\downarrow}$ show visible distinction. With the parallel magnetization in Figure 5a, the $E_{CBM\uparrow}$ of bilayer CrSBr is lower than $E_{CBM\downarrow}$ so the electrons trend to transfer from graphene to spin-up CBM in CrSBr, resulting in the high transmission probability of up states in sf-MTJ under PC. On the contrary, with the antiparallel magnetization in Figure 5b, $E_{CBM\uparrow}$ and $E_{CBM\downarrow}$ are much closer but $E_{CBM\downarrow}$ is lower. This may come from the imperfect antiparallel magnetization of CrSBr [35]. Thus, the electrons trend to transfer from graphene to spin-down CBM in CrSBr, but the tendency is weaker. The conclusions elucidate the reason why Figure 4a has higher transmission spots compared to Figure 4d and why the TMR is not large enough.

The local density of states (LDOS) is displayed in Figure 6 which could help to understand the process of transmission. At first, Figure 6a shows that when the sf-MTJ is in PC, the spin-up electron states in both CrSBr layers can be seen as metallic, because there is a high density of states near the Fermi level in the bilayer CrSBr. It can be deduced that the transmission performance of spin-up electrons is excellent. In contrast, Figure 6b shows that the spin-down electrons are strongly scattered. In Figure 6c or Figure 6d, only the right or left layer has states near the Fermi level, which shows a clear dependence on the spin polarization as well as indicates the scattering of electrons. In general, the up electrons in PC have a good transmission that others do not, so the obvious TMR effect emerges.

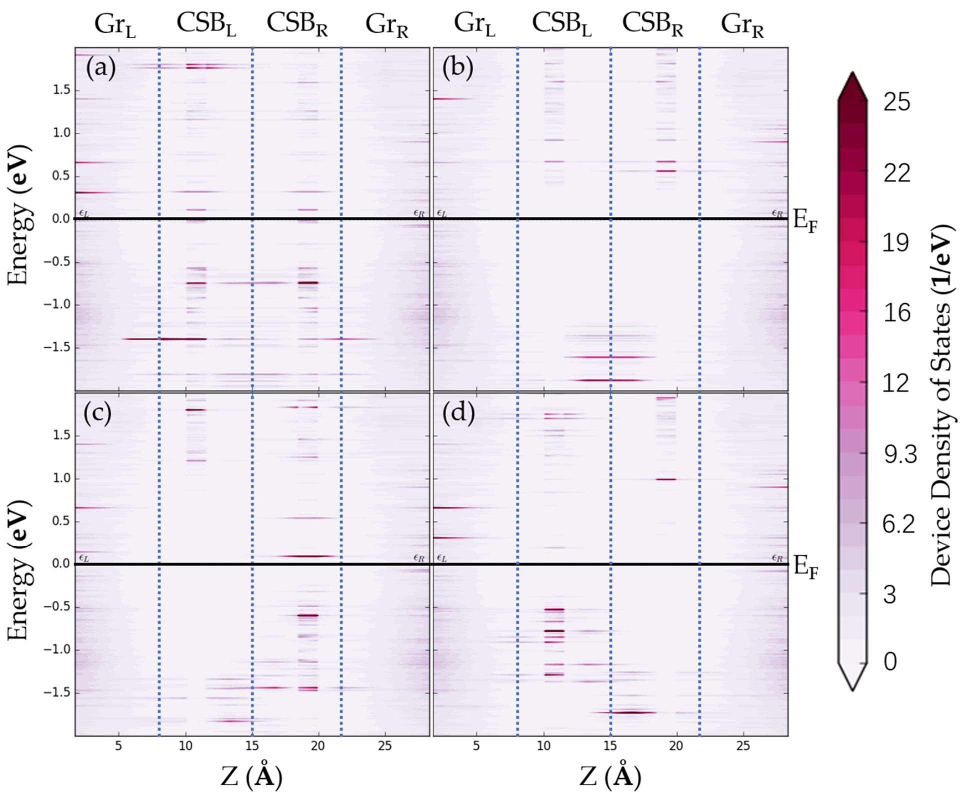

Figure 6. The local density of the states of the sf-MTJ based on bilayer CrSBr. (**a**) Up states in PC; (**b**) Down states in PC; (**c**) Up states in APC; and (**d**) Down states in APC. The vertical axis is the electron energy levels in which the Fermi level is set as 0 eV. The horizontal axis is the position of the device along the transmission direction. Different layers of the device marked above the figure by Gr_L (the graphene on the left); CSB_L (the left layer of the bilayer CrSBr); CSB_R (the right layer of the bilayer CrSBr); and Gr_R (the graphene on the left). Red colors indicate a high density of states. The figures are the calculated results of modeling.

Subsequently, we will discuss the giant TMR of sf-MTJs with four-layer and six-layer CrSBr. Like the two-layer device, we also obtained the transmission spectra. The transmission probabilities of electrons in APC are tiny, leading to negligible G_{AP}. That is one of the factors to the giant TMR values of the two devices (above $10^7\%$ and $10^5\%$). However, the spectra of APC carry little information for the lack of spots with high transmission probability. Therefore, we only provide the transmission spectra of spin-up electrons in PC that have distinct transmission characteristics to illustrate the giant TMRs in Figure 7a,b.

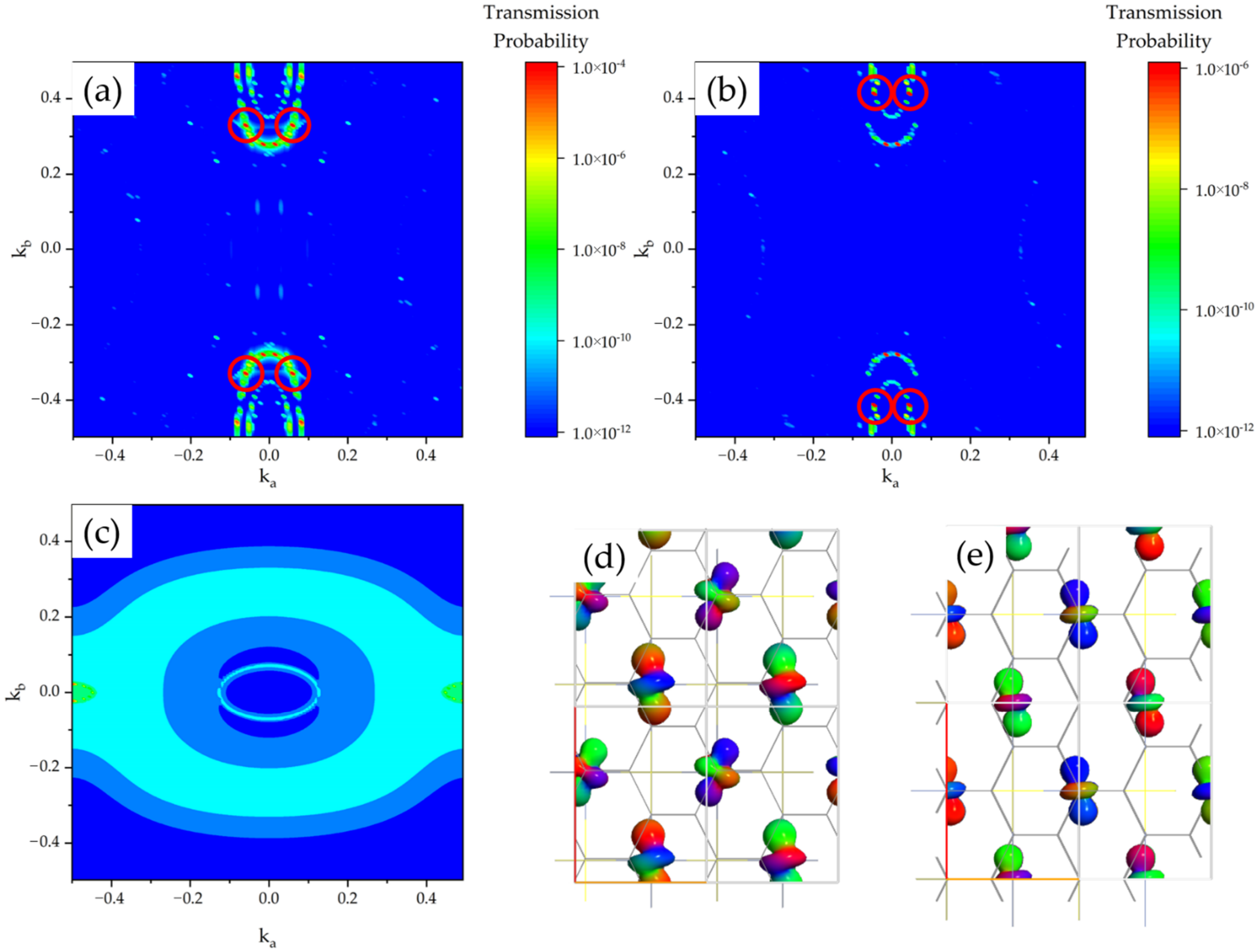

Figure 7. (**a**) Transmission spectrum of up states in 4-layer sf-MTJ under PC; (**b**) Transmission spectrum of up states in 6-layer sf-MTJ under PC. The spots with highest transmission probabilities are circled by red; (**c**) Transmission spectrum of graphene electrodes. Transmission spectra in the figure represent the transmission probabilities of electrons with different transverse Bloch wave vectors; (**d**,**e**) The transmission eigenstates of the spots with highest probability in (**a**,**b**) from the c axis perspective. The figures are the calculated results of the modeling.

Compared with Figure 4a, The transmission characteristics apart from the surrounding regions of the highest transmission probability in Figure 7a are more indistinctive. To verify the fact that the difference is independent from graphene electrodes, the transmission spectrum of the electrodes is calculated and presented in Figure 7c. The spectrum basically consists of characteristics of Δ_1 electrons, which are circular around the center. In addition, there is also small transmission at the midpoints of the left and right sides coming from the straining of the graphene when building the heterostructure. The features of graphene electrodes are relatively obvious in Figure 4a, but not in Figure 7a, meaning that four-layer

CrSBr entirely dominates the transmission. The eigenstates of the highest transmissions in the red circles can be seen in Figure 7d, similarly with Figure 4e. The eigenstates mainly originate from Δ_2 electrons with some deviation towards the lattice of graphene, suggesting that the graphene/CrSBr interfaces have a modest effect on transmission.

The transmission spectrum of the sf-MTJ based on six-layer CrSBr is purer in Figure 7b than in Figure 7a. The other transmission channels are lesser and the filtering of Δ_2 electrons is better. It is worth noting that the spots with the highest transmission have an upward shift. This may come from the increase in the thickness of CrSBr. With a six-layer CrSBr, the influence of the graphene/interface is weaker and the influence of inner layers is stronger, arousing the shift of the red spots in Figure 7b. The eigenstates of the highest transmission, presented in Figure 7e, also support the deduction. The eigenstates in Figure 7e are also mainly Δ_2 electrons but they tend to be more orderly and the deviation towards graphene is smaller than in Figure 7d.

4. Materials and Methods

All the computed results were obtained by first-principles calculations based on the quantum atomistix toolkit (quantumatk) [50] and Vienna Ab initio Simulation Package (vasp) code [51]. The electrostatic potential and band structure calculations were performed by projector augmented wave (PAW) method [52] in vasp. Considering the fact that the Perdew–Burke–Ernzerhof (PBE) functional [53] usually underestimates the band gap, we used a hybrid functional in the scheme of HSE06 [49] to perform the computation. The energies converged to 10^{-5} eV, the cut-off energy was set to 400 eV and the thickness of the vacuum layer along the c direction was 10 Å. In all the calculations in our work, the vdW forces were considered by the DFT-D3 method [44].

The optimizations and transmissions were implemented in quantumatk, based on DFT [54] in combination with the nonequilibrium Green's function (NEGF) [55,56]. The simulations in our work were performed at 0 K. A cut-off energy of 105 Hartree and a Γ-centered k-point mesh of $6 \times 8 \times 1$ in the scheme of the Monkhorst–Pack were used in the optimization. The forces converged towards 0.01 eV/Å. In the transmission calculations, the k points along the c directions should have been greater and therefore, the k-point mesh was set to $6 \times 8 \times 741$. The spin-resolved conductance is calculated by the Landauer conductance formula:

$$G_\sigma = \frac{e^2}{h} \sum_{k_{||}, j} T^{+}\left(k_{||}, j\right) \tag{1}$$

where σ is the spin index representing up ($\uparrow$) and down ($\downarrow$) and G_σ is the conductance. The transverse Bloch wave vector is $k_{||}$ which is equal to (k_a, k_b). The symbol j represents the Bloch state for a certain $k_{||}$ and T^{+} is the transmission probability along the positive direction from the left to right electrode.

5. Conclusions

In conclusion, we designed a new 2D sf-MTJ based on two, four and six layers of A-type antiferromagnetic CrSBr and graphene, connected with vdW forces. The sf-MTJ has a stable structure and presents a giant TMR effect with TMR values that are as high as 330%, 2×10^7% and 10^5% depending on the number of CrSBr layers. The transmission spectra of the sf-MTJs were calculated and the spin-up and spin-down states showed significant differences in transmission. We analyzed the underlying mechanism of the high TMR through the transmission spectra, eigenstates, electrostatic potentials and LDOS of the two-layer device. The results show that the device had a good filtering characteristic of Δ_2 electrons which dominated the transmission. The HSE06 band structures confirmed the electron transfer from graphene to CrSBr in the device and demonstrated the details in transmission spectra. The LDOS presented the electron distribution in the device and supported the existence of the TMR effect.

The sf-MTJs with the four-layer and six-layer CrSBr turned out to have a bigger TMR because a thicker barrier had a better scattering of tunneling electrons for the semiconducting property. This was reflected in the transmission spectra for the tiny transmission probabilities in APC. Considering the fact that CrSBr is an air-stable 2D vdW intrinsic magnet, which is easy to prepare and has a high Néel temperature, our results demonstrate that the sf-MTJ with the CrSBr barrier (especially four layers) and a graphene electrode may have a prospect in experiments and applications.

Author Contributions: Conceptualization, H.L.; methodology, H.L. and Y.-Y.L.; software, Y.-Y.L. and H.W. (Haibin Wu); validation, Y.-Y.L. and H.W. (Hongyu Wen); formal analysis, H.L., H.W. (Hongyu Wen) and Y.Z.; investigation, H.L. and H.W. (Hongyu Wen); resources, H.L.; data curation, H.W. (Hongyu Wen) and Y.-Y.L.; writing—original draft preparation, H.L.; writing—review and editing, Y.-Y.L.; visualization, H.L.; supervision, Z.W., H.W. (Haibin Wu) and J.X.; project administration, H.W. (Hongyu Wen), Y.-Y.L. and Y.Z.; funding acquisition, H.W. (Hongyu Wen), Y.Z. and Y.-Y.L. All authors have read and agreed to the published version of the manuscript.

Funding: This work was funded by the National Natural Science Foundation of China (Grant No. 12104448, 11904360, 62174155 and 12004375), the Strategic Priority Research Program of the Chinese Academy of Sciences (Grant No. XDB43000000) and the CAS-JSPS Cooperative Research Project (No. GJHZ2021131).

Data Availability Statement: The data supporting the reported results of the study are available from the corresponding author upon reasonable request.

Conflicts of Interest: The authors declare no conflict of interest. The funders had no role in the design of the study; in the collection, analyses, or interpretation of data; in the writing of the manuscript; or in the decision to publish the results.

References

1. Julliere, M. Tunneling between ferromagnetic films. *Phys. Lett. A* **1975**, *54*, 225–226. [CrossRef]
2. Wolf, S.; Awschalom, D.; Buhrman, R.; Daughton, J.; Molnár, S.; Roukes, M.; Chtchelkanova, A.; Treger, D.M. Spintronics: A Spin-Based Electronics Vision for the Future. *Science* **2001**, *294*, 1488–1495. [CrossRef] [PubMed]
3. Yang, S.; Zhang, J. Current Progress of Magnetoresistance Sensors. *Chemosensors* **2021**, *9*, 211. [CrossRef]
4. Swagten, H.J.M.; Paluskar, P. Magnetic Tunnel Junctions. *Mater. Today* **2016**, *9*, 36–45.
5. Baibich, M.; Broto, J.-M.; Fert, A.F.; F, N.; Petroff, F.; Etienne, P.E.; Creuzet, G.; Friederich, A.; Chazelas, J. Giant Magnetoresistance of (001)Fe/(001)Cr Magnetic Superlattices. *Phys. Rev. Lett.* **1988**, *61*, 2472–2475. [CrossRef]
6. Ennen, I.; Kappe, D.; Rempel, T.; Glenske, C.; Hutten, A. Giant Magnetoresistance: Basic Concepts, Microstructure, Magnetic Interactions and Applications. *Sensors* **2016**, *16*, 904. [CrossRef]
7. Dieny, B. Giant Magnetoresistance in Spin-Valve Multi-layers. *J. Magn. Magn. Mater.* **1994**, *136*, 335–359. [CrossRef]
8. Svalov, A.V.; Savin, P.; Kurlyandskaya, G.; Gutierrez, J.; Barandiaran, J.M.; Vas'kovskiy, V.O. Spin-valve structures with Co-Tb-based multilayers. *IEEE Trans. Magn.* **2002**, *38*, 2782–2784. [CrossRef]
9. Parkin, S. Giant Magnetoresistance in Magnetic Nanostructures. *Annu. Rev. Mater. Sci.* **2003**, *25*, 357–388. [CrossRef]
10. Zheng, C.; Zhu, P.K.; Cardoso, S.; Chang, J.-Y.; Davies, J.; Eames, P.; Freitas, P.; Kazakova, O.; Kim, C.; Leung, C.-W.; et al. Magnetoresistive Sensor Development Roadmap (Non-Recording Applications). *IEEE Trans. Magn.* **2019**, *55*, 1–30. [CrossRef]
11. Grabchikov, S.S.; Trukhanov, A.; Trukhanov, S.; Kazakevich, I.; Solobay, A.A.; Erofeenko, V.T.; Vasilenkov, N.V.; Volkova, O.S. Effectiveness of the magnetostatic shielding by the cylindrical shells. *J. Magn. Magn. Mater.* **2015**, *398*, 49–53. [CrossRef]
12. Trukhanov, A.; Grabchikov, S.S.; Solobai, A.; Chushkova, D.; Trukhanov, S.; Trukhanova, E.L. AC and DC-shielding properties for the $Ni_{80}Fe_{20}$/Cu film structures. *J. Magn. Magn. Mater.* **2017**, *443*, 142–148. [CrossRef]
13. Ajayan, P.; Kim, P.; Banerjee, K. Two-dimensional van der Waals materials. *Phys. Today* **2016**, *69*, 38–44. [CrossRef]
14. Dayen, J.F.; Ray, S.; Karis, O.; Vera-Marun, I.; Kamalakar, M.V. Two-dimensional van der Waals spinterfaces and magnetic-interfaces. *Appl. Phys. Rev.* **2020**, *7*, 11303. [CrossRef]
15. Ahn, E. 2D materials for spintronic devices. *Npj 2D Mater. Appl.* **2020**, *4*, 17. [CrossRef]
16. Gong, C.; Li, L.; Li, Z.; Ji, H.; Stern, A.; Xia, Y.; Cao, T.; Bao, W.; Wang, C.; Wang, Y.; et al. Discovery of intrinsic ferromagnetism in two-dimensional van der Waals crystals. *Nature* **2017**, *546*, 265–269. [CrossRef] [PubMed]
17. Huang, B.; Clark, G.; Navarro-Moratalla, E.; Klein, D.; Cheng, R.; Seyler, K.; Zhong, D.; Schmidgall, E.; McGuire, M.; Cobden, D.; et al. Layer-dependent Ferromagnetism in a van der Waals Crystal down to the Monolayer Limit. *Nature* **2017**, *546*, 270–273. [CrossRef]
18. Deng, Y.; Yu, Y.; Song, Y.; Zhang, J.; Wang, N.; Wu, Y.; Zhu, J.; Wang, J.; Chen, X.; Zhang, Y. Gate-tunable Room-temperature Ferromagnetism in Two-dimensional Fe_3GeTe_2. *Nature* **2018**, *563*, 94–99. [CrossRef]
19. Huang, Y.; Chen, W.; Wee, A. Two-dimensional magnetic transition metal chalcogenides. *SmartMat* **2021**, *2*, 139–153. [CrossRef]
20. Loong, L.; Lee, W.; Qiu, X.; Yang, P.; Kawai, H.; Saeys, M.; Ahn, J.-H.; Yang, H. Flexible MgO Barrier Magnetic Tunnel Junctions. *Adv. Mater.* **2016**, *28*, 4983–4990. [CrossRef]

21. Knudde, S.; Farinha, G.; Leitao, D.; Ferreira, R.; Cardoso, S.; Freitas, P. AlOx barrier growth in magnetic tunnel junctions for sensor applications. *J. Magn. Magn. Mater.* **2016**, *412*, 181–184. [CrossRef]
22. Diao, Z.; Panchula, A.; Ding, Y.; Pakala, M.; Wang, S.; Li, Z.; Apalkov, D.; Nagai, H.; Driskill-Smith, A.; Wang, L.-C.; et al. Spin transfer switching in dual MgO magnetic tunnel junctions. *Appl. Phys. Lett.* **2007**, *90*, 132508. [CrossRef]
23. Park, W.; Moon, K. Switchable Voltage Offset in a Heusler Alloy-based Magnetic Tunnel Junction. *J. Magn. Magn. Mater.* **2018**, *469*, 274–278. [CrossRef]
24. Lu, H.; Robertson, J.; Naganuma, H. Comparison of hexagonal boron nitride and MgO tunnel barriers in Fe, Co magnetic tunnel junctions. *Appl. Phys. Rev.* **2021**, *8*, 31307. [CrossRef]
25. Yuasa, S.; Djayaprawira, D. Giant tunnel magnetoresistance in magnetic tunnel junctions with a crystalline MgO(001) barrier. *J. Phys. D Appl. Phys.* **2007**, *40*, 337–354. [CrossRef]
26. Worledge, D.; Geballe, T. Magnetoresistive double spin filter tunnel junction. *J. Appl. Phys.* **2000**, *88*, 5277–5279. [CrossRef]
27. Miao, G.-X.; Müller, M.; Moodera, J. Magnetoresistance in Double Spin Filter Tunnel Junctions with Nonmagnetic Electrodes and its Unconventional Bias Dependence. *Phys. Rev. Lett.* **2009**, *102*, 76601. [CrossRef] [PubMed]
28. Song, T.; Cai, X.; Tu, W.-Y.; Zhang, X.; Huang, B.; Wilson, N.; Seyler, K.; Zhu, L.; Taniguchi, T.; Watanabe, K.; et al. Giant Tunneling Magnetoresistance in Spin-Filter van der Waals Heterostructures. *Science* **2018**, *360*, 1214–1218. [CrossRef]
29. Jin, W.; Kim, H.; Ye, Z.; Li, S.; Rezaie, P.; Diaz, F.; Siddiq, S.; Wauer, E.; Yang, B.; Chenghe, L.; et al. Raman fingerprint of two terahertz spin wave branches in a two-dimensional honeycomb Ising ferromagnet. *Nat. Commun.* **2018**, *9*, 5122. [CrossRef]
30. Rahman, S.; Torres, J.F.; Khan, A.; Lu, Y. Recent Developments in van der Waals Antiferromagnetic 2D Materials: Synthesis, Characterization, and Device Implementation. *ACS Nano* **2021**, *15*, 17175–17213. [CrossRef]
31. Parkin, S.; Kaiser, C.; Panchula, A.; Rice, P.; Hughes, B.; Samant, M.; Yang, S.-H. Giant Tunneling Magnetoresistance at Room Temperature with MgO(100) Tunnel Barriers. *Nat. Mater.* **2005**, *3*, 862–867. [CrossRef] [PubMed]
32. McGuire, M.; Clark, G.; Santosh, K.; Chance, W.; Jellison, G.E., Jr.; Cooper, V.; Xu, X.; Sales, B. Magnetic Behavior and Spin-Lattice Coupling in Cleavable, van der Waals Layered $CrCl_3$ Crystals. *Phys. Rev. Mater.* **2017**, *1*, 14001. [CrossRef]
33. Zhang, S.; Wang, R.; Wang, X.; Wei, B.; Chen, B.; Wang, H.; Shi, G.; Wang, F.; Jia, B.; Ouyang, Y.; et al. Experimental Observation of the Gate-Controlled Reversal of the Anomalous Hall Effect in the Intrinsic Magnetic Topological Insulator $MnBi_2Te_4$ Device. *Nano Lett.* **2019**, *20*, 709714. [CrossRef] [PubMed]
34. Huang, X.; Tang, Y.; Dong, S. Strain-engineered A-type antiferromagnetic order in $YTiO_3$: A first-principles calculation. *J. Appl. Phys.* **2013**, *113*, 17E108. [CrossRef]
35. Telford, E.; Dismukes, A.; Lee, K.; Cheng, M.; Wieteska, A.; Bartholomew, A.; Chen, Y.-S.; Xu, X.; Pasupathy, A.; Zhu, X.; et al. Layered Antiferromagnetism Induces Large Negative Magnetoresistance in the van der Waals Semiconductor CrSBr. *Adv. Mater.* **2020**, *32*, 2003240. [CrossRef]
36. Zubar, T.; Fedosyuk, V.; Trukhanov, S.; Chushkova, D.; Michels, D.; Lyakhov, D.; Trukhanov, A. Method of surface energy investigation by lateral AFM: Application to control growth mechanism of nanostructured NiFe films. *Sci. Rep.* **2020**, *10*, 14411. [CrossRef]
37. Sharko, S.; Serokurova, A.; Novitskii, N.; Ketsko, V.; Smirnova, M.; Almuqrin, A.; Trukhanov, S.; Trukhanov, A. A New Approach to the Formation of Nanosized Gold and Beryllium Films by Ion-Beam Sputtering Deposition. *Nanomaterials* **2022**, *12*, 470. [CrossRef]
38. Jiang, Z.; Wang, P.; Xing, J.; Jiang, X.; Zhao, J. Screening and Design of Novel 2D Ferromagnetic Materials with High Curie Temperature above Room Temperature. *ACS Appl. Mater. Interfaces* **2018**, *10*, 39032–39039. [CrossRef]
39. Ye, C.; Wang, C.; Wu, Q.; Liu, S.; Zhou, J.; Wang, G.; Söll, A.; Sofer, Z.; Yue, M.; Liu, X.; et al. Layer-Dependent Interlayer Antiferromagnetic Spin Reorientation in Air-Stable Semiconductor CrSBr. *ACS Nano*, 2022; *in press*. [CrossRef]
40. Trukhanov, S.; Trukhanov, A.; Turchenko, V.; Trukhanov, A.V.; Chushkova, D.; Trukhanova, E.L.; Ivanov, V.M.; Salem, M.; Kostishyn, V.G.; Panina, L.; et al. Polarization origin and iron positions in indium doped barium hexaferrites. *Ceram. Int.* **2017**, *44*, 290–300. [CrossRef]
41. Turchenko, V.; Trukhanov, S.; Kostishin, V.; Damay, F.; Porcher, F.; Klygach, D.; Vakhitov, M.; Matzui, L.; Yakovenko, O.; Bozzo, B.; et al. Impact of In^{3+} cations on structure and electromagnetic state of M-type hexaferrites. *J. Energy Chem.* **2021**, *69*, 667–676. [CrossRef]
42. Huang, B.; McGuire, M.; May, A.; Xiao, D.; Jarillo-Herrero, P.; Xu, X. Emergent phenomena and proximity effects in two-dimensional magnets and heterostructures. *Nat. Mater.* **2020**, *19*, 1276–1289. [CrossRef] [PubMed]
43. Wang, H.; Qi, J.; Qian, X. Electrically tunable high Curie temperature two-dimensional ferromagnetism in van der Waals layered crystals. *Appl. Phys. Lett.* **2020**, *117*, 83102. [CrossRef]
44. Grimme, S.; Antony, J.; Ehrlich, S.; Krieg, H. A Consistent and Accurate Ab Initio Parametrization of Density Functional Dispersion Correction (DFT-D) for the 94 Elements H-Pu. *J. Chem. Phys.* **2010**, *132*, 154104. [CrossRef] [PubMed]
45. Troyanchuk, I.; Trukhanov, S.; Shapovalova, E.; Khomchenko, V.; Tovar, M.; Szymczak, H. The influence of oxygen vacancies on the magnetic state of $La_{0.50}D_{0.50}MnO_{3-\gamma}$ (D = Da, Sr) manganites. *J. Exp. Theor. Phys.* **2003**, *96*, 1055–1064. [CrossRef]
46. Trukhanov, S.; Bushinsky, M.; Troyanchuk, I.; Szymczak, H. Magnetic ordering in $La_{1-x}Sr_xMnO_{3-x/2}$ anion-deficient manganites. *J. Exp. Theor. Phys.* **2004**, *99*, 756–765. [CrossRef]
47. Tiusan, C.; Greullet, F.; Hehn, M.; Montaigne, F.; Andrieu, S.; Schuhl, A. Spin tunnelling phenomena in single-crystal magnetic tunnel junction systems. *J. Phys. Condens. Matter.* **2007**, *19*, 165201. [CrossRef]

48. Stewart, D. New Type of Magnetic Tunnel Junction Based on Spin Filtering through a Reduced Symmetry Oxide: FeCo | $Mg_3B_2O_6$ | FeCo. *Nano Lett.* **2009**, *10*, 263–267. [CrossRef]
49. Heyd, J.; Scuseria, G.E.; Ernzerhof, M. Hybrid functionals based on a screened Coulomb potential. *J. Chem. Phys.* **2006**, *124*, 8207–8215. [CrossRef]
50. Smidstrup, S.; Markussen, T.; Vancraeyveld, P.; Wellendorff, J.; Schneider, J.; Gunst, T.; Verstichel, B.; Stradi, D.; Khomyakov, P.; Vej-Hansen, U.; et al. QuantumATK: An integrated platform of electronic and atomic-scale modelling tools. *J. Phys. Condens. Matter.* **2019**, *32*, 15901. [CrossRef]
51. Kresse, G.; Furthmüller, J. Efficient iterative schemes for ab initio total-energy calculations using a plane-wave basis set. *Phys. Rev. B* **1996**, *55*, 11169–11174. [CrossRef] [PubMed]
52. Blöchl, P. Projector Agmented-Wave Method. *Phys. Rev. B* **1994**, *50*, 17953–17979. [CrossRef] [PubMed]
53. Perdew, J.; Burke, K.; Ernzerhof, M. Generalized Gradient Approximation Made Simple. *Phys. Rev. Lett.* **1996**, *77*, 3865–3868. [CrossRef] [PubMed]
54. Smidstrup, S.; Stradi, D.; Wellendorff, J.; Khomyakov, P.; Vej-Hansen, U.; Lee, M.-E.; Ghosh, T.; Jónsson, E.; Jonsson, H.; Stokbro, K. First-principles Green's-function method for surface calculations: A pseudopotential localized basis set approach. *Phys. Rev. B* **2017**, *96*, 195309. [CrossRef]
55. Marmolejo-Tejada, J.; Dolui, K.; Lazic, P.; Chang, P.-H.; Smidstrup, S.; Stradi, D.; Stokbro, K.; Nikolic, B. Proximity Band Structure and Spin Textures on Both Sides of Topological-Insulator/Ferromagnetic-Metal Interface and Their Charge Transport Probes. *Nano Lett.* **2017**, *17*, 5626–5633. [CrossRef]
56. Brandbyge, M.; Mozos, J.-L.; Ordejon, P.; Taylor, J.; Stokbro, K. Density-functional method for nonequilibrium electron transport. *Phys. Rev. B* **2001**, *65*, 165401. [CrossRef]